Published online 7 August 2021

Nucleic Acids Research, 2021, Vol. 49, No. 15 **8811–8821**
https://doi.org/10.1093/nar/gkab666

An induced-fit *de novo* initiation mechanism suggested by a pestivirus RNA-dependent RNA polymerase

Bu-Yu Zhang[1,2,†], Weichi Liu[1,2,*,†], Hengxia Jia[1,2], Guoliang Lu[1] and Peng Gong[1,3,*]

[1]Key Laboratory of Special Pathogens and Biosafety, Wuhan Institute of Virology, Center for Biosafety Mega-Science, Chinese Academy of Sciences, No.44 Xiao Hong Shan, Wuhan, Hubei 430071, China, [2]University of Chinese Academy of Sciences, Beijing 100049, China and [3]Drug Discovery Center for Infectious Diseases, Nankai University, Tianjin 300350, China

Received May 22, 2021; Revised July 15, 2021; Editorial Decision July 15, 2021; Accepted August 06, 2021

ABSTRACT

Viral RNA-dependent RNA polymerases (RdRPs) play central roles in the genome replication and transcription processes of RNA viruses. RdRPs initiate RNA synthesis either in primer-dependent or *de novo* mechanism, with the latter often assisted by a 'priming element' (PE) within the RdRP thumb domain. However, RdRP PEs exhibit high-level structural diversity, making it difficult to reconcile their conserved function in *de novo* initiation. Here we determined a 3.1-Å crystal structure of the *Flaviviridae* classical swine fever virus (CSFV) RdRP with a relative complete PE. Structure-based mutagenesis in combination with enzymology data further highlights the importance of a glycine residue (G671) and the participation of residues 665–680 in RdRP initiation. When compared with other representative *Flaviviridae* RdRPs, CSFV RdRP PE is structurally distinct but consistent in terminal initiation preference. Taken together, our work suggests that a conformational change in CSFV RdRP PE is necessary to fulfill *de novo* initiation, and similar 'induced-fit' mechanisms may be commonly taken by PE-containing *de novo* viral RdRPs.

INTRODUCTION

RNA-dependent RNA polymerases (RdRPs) carrying out RNA-directed RNA synthesis in viral RNA genome replication and transcription play central roles in the life cycle of RNA viruses. Efficient and faithful RdRP initiation at preferred sites is essential for the integrity of viral RNA genome and production of accurate transcripts. Similar to DNA-dependent RNA polymerases, RdRPs undergo relatively unstable initiation before entering an elongation phase that allows synthesis of thousands of nucleotides in a processive manner (1–3). As different initiation mechanisms of RNA synthesis exist in RNA viruses, it is conceivable that unique elements, either acting intra- or inter-molecularly, can be utilized by RdRPs to ensure necessary precision and efficiency at initiation. For primer-dependent viral RdRPs, either a virally-encoded VPg protein (viral protein genome-linked), an RNA oligonucleotide synthesized by primase-like viral enzymes, or a capped RNA oligonucleotide generated by a 'cap-snatching' process can serve as the primer to guide RdRP initiation (4–6). For the majority of RdRPs utilizing *de novo* initiation mechanisms, a substructure within the RdRP proteins, herein termed 'priming element' (PE), can approach the active site and interact with the RNA template and the initiating NTPs (7–10), achieving initiation in a relatively self-sufficient manner. Being the most conserved enzyme encoded by RNA viruses, viral RdRP contains a polymerase core that structurally resembles an encircled human right hand comprising palm, fingers, and thumb domains surrounding the active site, with unique fingers-thumb interactions to make the encirclement (11–14). Seven catalytic motifs A–G surround the active site with A-E in the most conserved palm and F/G in the fingers, while PE is usually a component of the thumb (13–16).

RdRPs of several virus families, including *Flaviviridae*, *Cystoviridae* and *Orthomyxoviridae*, represent classical PE-containing RdRPs capable of *de novo* initiation. Crystal structures of RdRP initiation complexes (ICs) from the *Cystoviridae* bacteriophage ϕ6 and the *Flaviviridae* hepatitis C virus (HCV) revealed very similar initiation mechanisms with rather distinct PE substructures. The side chains of ϕ6

*To whom correspondence should be addressed. Tel: +86 27 87197578; Fax: +86 27 87197578; Email: gongpeng@wh.iov.cn
Correspondence may also be addressed to Weichi Liu. Email: liuweichi1990@163.com
†The authors wish it to be known that, in their opinion, the first two authors should be regarded as Joint First Authors.
Present address: Guoliang Lu, State Key Laboratory of Genetic Engineering, School of Life Sciences, Zhongshan Hospital, Fudan University, Shanghai 200438, China.

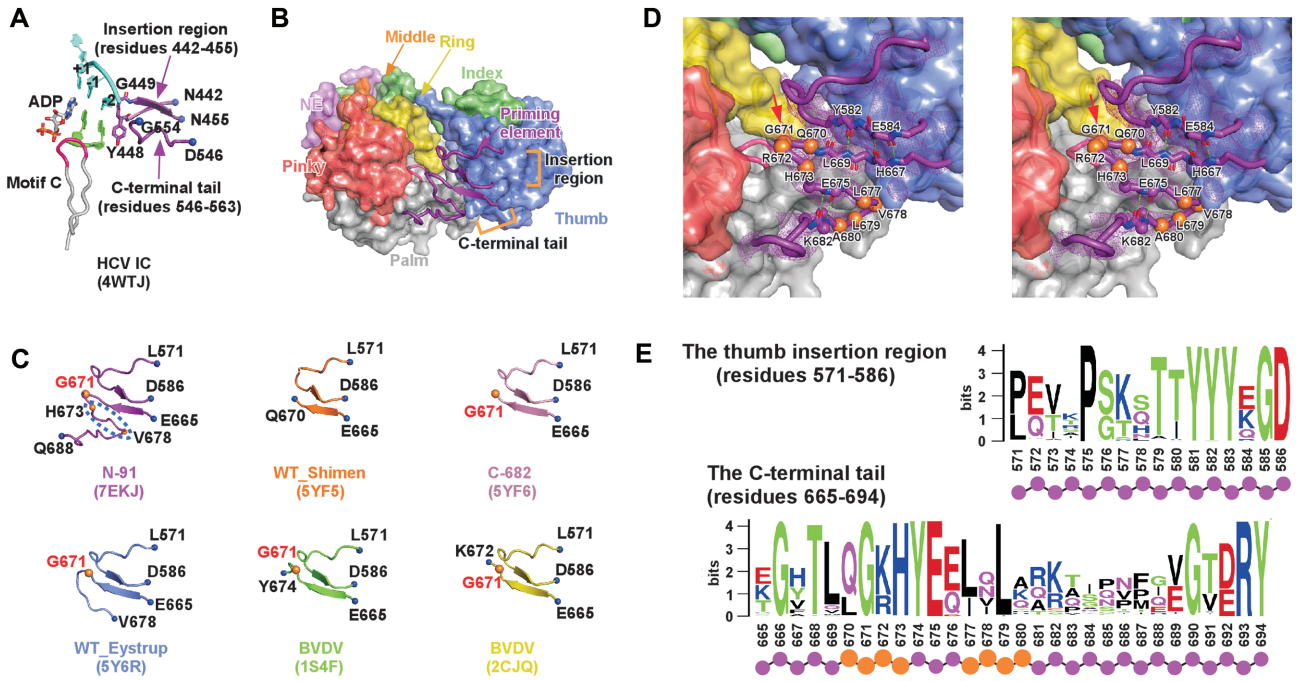

Figure 1. A crystal structure of CSFV NS5B with a relatively complete PE substructure. (**A**) The crystal structure of HCV NS5B IC (PDB entry: 4WTJ). Template RNA is in cyan, dinucleotide primer is in green, PE is in purple, motif C CGDD sequence is in magenta and the other region of motif C is in gray. ADP and residues Y448 and G449 are shown as sticks, and the α-carbon atoms of residues N442, N455, D546 and G554 are shown as blue spheres. (**B**) A global view of CSFV NS5B N-91. Except for the motif C CGDD sequence and PE, cartoon representations are masked by semi-transparent surface representations. Coloring scheme: PE—purple, CGDD sequence—magenta, N-terminal extension (NE)—violet, palm—gray, index/middle/ring/pinky fingers—green/orange/yellow/pink, thumb—slate. (**C**) A comparison of the pestivirus RdRP PE structures with PDB entries listed. The α-carbon atoms of the residues at the ends of the thumb insertion region and C-terminal tail of PE are shown as blue spheres, α-carbon atoms of G671 are shown as orange spheres, and α-carbon atoms of H673/V678 of N-91 PE structure are also shown as orange spheres. The region of residues 673–678 is highlight with a blue dotted circle. Top row: CSFV NS5B structures from Shimen strain (N-91, WT and C-682); bottom row: CSFV NS5B WT (Eystrup strain) and representative BVDV NS5B constructs. (**D**) Stereo-pair images of the N-91 structure zoomed in around PE with 3500 K composite SA-omit $2F_o - F_c$ electron density map (contoured at 1.5 σ) overlaid. The coloring scheme and representations are the same as in panel B. The α-carbon atoms of residues 670–683 are shown in spheres with those in the β-turns colored in orange. Characteristic hydrogen bonding interactions maintaining the β-type structures of the PE C-terminal tail are shown as green dashed lines. (**E**) A conservation analysis of the pestivirus PE. Sequence logos generated using a multiple-sequence alignment of 219 NS5B sequences of pestivirus (http://weblogo.berkeley.edu/). Top panel: the thumb insertion (residues 571–586), bottom panel: the C-terminal tail (residues 665–694).

RdRP Q629 and Y630 in a short helix form hydrophobic interactions with the –1 template nucleotide and the priming NTP, respectively (7), while in the dinucleotide-derived IC the side chain of HCV RdRP Y448 and peptide plane of Y448-G449 in the tip of a β-turn interact with the -2 template nucleotide and the –2 nucleotide of the priming dinucleotide, respectively (8) (Figure 1A). These PE substructures provide a relatively flat-shape surface at the immediate upstream of the RdRP initiation site, thus not only stabilizing the interactions involving the template strand and the NTP/dinucleotide substrates but also restricting the placement of the 3′-end of the template strand for precise terminal initiation.

The *Flaviviridae* family currently includes *Hepacivirus*, *Pegivirus*, *Pestivirus* and *Flavivirus* genera. Based on both structural and protein sequence information, three representative PE substructure types exist in *Flavivridae* RdRPs. The first type is represented by that of the *Hepacivirus* HCV NS5B containing a β-hairpin (residues 442–455, including the aforementioned YG sequence) as an insertion in the thumb and a C-terminal tail (residues 546–563) co-folding with the β-hairpin through parallel β-type interactions (8,11). The second type is represented by that of the *Pestivirus* classical swine fever virus (CSFV) or bovine viral diarrhea virus (BVDV) NS5B, with a similar two-segment combination. By contrast, the β-hairpin counterpart (residues 571–586 in CSFV) in the pestivirus RdRP adopts a loop conformation and is about 9-Å shorter than the HCV β-hairpin (17,18), while the pestivirus C-terminal tail (residues 665–694) interacts with this loop through antiparallel β-type interactions. The third type is represented by that of the *Flavivirus* Japanese encephalitis virus (JEV) or dengue virus (DENV) NS5, having a single thumb insertion segment (residues 790–813 in JEV) also known as the 'priming loop' (19,20). It is expected that these structurally diverse PEs can facilitate *de novo* initiation in a somehow similar manner as observed in the comparison of HCV and ϕ6 IC structures. However, the mechanistic details remain elusive due to the lack of both structural and enzymology data, in particular in the *Pestivirus* and *Flavivirus* genera.

In this work, we report a 3.1-Å resolution crystal structure of CSFV NS5B, and the structure reveals previously unidentified structural information for residues 673–688 in the C-terminal tail of PE. This region forms additional antiparallel β-type interactions with residues 667–670 and contributes to the structural integrity of PE. Enzymology

Table 1. X-ray diffraction data collection and structure refinement statistics

PDB	7EKJ
Data collection[a]	
Space group	$P\,4_3\,2_1\,2$
Cell dimensions	
a, *b*, *c* (Å)	82.1, 82.1, 228.1
α, β, γ (°)	90, 90, 90
Resolution (Å)[b]	60.0–3.06 (3.17–3.06)
No. unique reflections	14,282
R_{merge}	0.084 (0.54)
R_{meas}	0.088 (0.57)
$CC_{1/2}$	0.986 (0.937)
I / σI	24.0 (3.3)
Completeness (%)	92.6 (74.5)
Redundancy	9.4 (8.9)
Structure refinement	
Resolution (Å)	3.06
No. unique reflections	14,197
R_{work}/R_{free}[c] (%)	26.8/28.3
No. atoms	
Protein	4,337
Ligand/Ion/Water	/ /
B-factors (Å^2)	
Protein	103.1
Ligand/Ion/Water	/ /
R.m.s. deviations	
Bond lengths (Å)	0.010
Bond angles (°)	1.330
Ramachandran stat.[d]	84.3/14.9/0.6/0.2

[a]One crystal was used for data collection.
[b]Values in parentheses are for highest-resolution shell.
[c]5% of data are taken for the R_{free} set.
[d]Values are in percentage and are for most favored, additionally allowed, generously allowed, and disallowed regions in Ramachandran plots, respectively.

characterization of WT NS5B and its PE mutants further suggests that structural dynamics of PE assisted by residue G671 is likely required to allow the 665–680 region of the C-terminal tail to approach the active site for efficient initiation. Further structural comparison combined with enzymology tests highlights the conformational adaptation of PE at initiation may widely exist in *de novo* viral RdRPs, thus providing an important reference to understand RdRP initiation in general.

MATERIALS AND METHODS

Plasmid construction and protein production

A pET26b-CSFV-NS5B (residues 1–694, Shimen strain) plasmid was used as the template for construction of all mutant plasmids by using site-directed, ligase-independent mutagenesis (SLIM) for deletions and QuikChange site-directed mutagenesis for point mutations as previously described, and each NS5B construct contains a C-terminal hexahistidine tag (18,21,22). Cell growth, isopropyl-β-D-thiogalactopyranoside (IPTG) induction, cell harvesting, cell lysis, protein purification and protein storage were performed as described previously (18). The HCV (BK strain) NS5B was prepared using a pET26b-based plasmid and *Escherichia coli* Rosetta (DE3) strain, and the bacteria was grown in terrific broth (TB) medium. Protein purification and storage for HCV NS5B were performed as previously described in the JEV NS5 study except that a 100 mM imidazole wash step was applied prior to the elution step of the Ni-affinity chromatography, MES (pH 6.5)/5% (vol./vol.) glycerol and Tris (pH 7.5)/500 mM NaCl/5% (vol/vol) glycerol were used for the cation-exchange and gel filtration columns, respectively (20). The yield is typically 3 mg of pure NS5B protein per liter of bacterial culture. The DENV serotype 2 (DENV2) NS5 protein preparation was performed as previously described (23). Protein concentrations were measured based on protein sequences by absorbance at 280 nm using molar extinction coefficients calculated by the ExPASy ProtParam program (http://web.expasy.org/protparam/).

Protein crystallization and structure determination

Crystals of CSFV NS5B N-91 were grown by sitting drop vapor diffusion at 16°C using 8 and 10 mg/ml protein. Within 2 weeks, lamellar crystals grew with a precipitant/well solution of 0.1 M sodium acetate trihydrate (pH 4.6) and 2.0 M ammonium sulfate. Crystals were transferred to a cryo-solution (precipitant solution supplemented with 25% (vol/vol) glycerol) by incremental buffer exchange prior to flash cooling in liquid nitrogen.

Single crystal X-ray diffraction data was collected at Shanghai Synchrotron Radiation Facility (SSRF) beamlines BL19U1 (wavelength = 0.9785 Å, temperature = 100 K). 180° of data were collected in 0.5° oscillation steps. Reflections were integrated, merged, and scaled using HKL2000 (24) (Table 1). The initial structure solution was obtained using the molecular replacement program PHASER using coordinates derived from a WT CSFV NS5B structure (PDB entry: 5YF5) as the search model (25). Manual model building and structure refinement were done using Coot and PHENIX, respectively (26,27). The 3500 K composite simulated-annealing omit $2F_o - F_c$ electron density map was generated using PHENIX. Unless otherwise indicated, protein structure superimpositions were carried out using the maximum-likelihood superpositioning program THESEUS (28).

RNA preparation

The 30-mer template strand RNA (T30) used for *in vitro* RdRP assays was chemically synthesized (Integrated DNA Technologies). The 32-mer and 34-mer template RNAs (T32, T34-1 and T34-2) were obtained by *in vitro* T7 RNA polymerase transcription/*glmS* ribozyme-based approach as previously described (29,30). The RNAs were purified by 12% (wt/vol) polyacrylamide/7 M urea gel electrophoresis. The target RNA was excised from the gel, electro-eluted by using an Elu-Trap device (GE Healthcare), precipitated by ethanol precipitation, dissolved and stored in an RNA annealing buffer (RAB) of 50 mM NaCl, 5 mM Tris (pH 7.5), 5 mM $MgCl_2$ at –80°C after a self-annealing process (a 3-min incubation at 95°C followed by snap-cooling to minimize intermolecular annealing). A 5′-phosphorylated G–G dinucleotide (pGG or P2, Jena Bioscience) was annealed to each template RNA at a 1.25:1 molar ratio via a 3-min incubation at 45°C followed by slow-cooling to room temperature in RAB to yield the template/P2 constructs.

In vitro de novo RdRP assays

For all *in vitro de novo* RdRP assays based on the dinucleotide (P2)-driven reactions, the CSFV NS5B reaction buffer contains 50 mM Tris (pH 7.0), 5 mM $MgCl_2$, 5 mM dithiothreitol (DTT) and 20 mM NaCl, the HCV NS5B reaction buffer contains 40 mM MES (pH 6.5), 2 mM $MgCl_2$, 5 mM DTT and 30 mM NaCl, and the DENV2 NS5 reaction buffer is the same as CSFV, except that Tris (pH 7.5) was used as the buffering agent. For the 9-mer product (P9)-containing EC (EC9) formation assay to achieve the P2-to-P9 conversion, a typical 20 μl reaction mixture containing 6 μM RdRP protein, 4 μM template/P2 construct (including 5 μM P2), 15 μM extra P2, 300 μM ATP, and 300 μM UTP in the corresponding reaction buffer, was incubated at 30°C for 45 min. Reaction quenching, denaturing polyacrylamide gel electrophoresis (PAGE), gel staining and quantitative analyses were performed as previously described (18,30). The Stains-All (Sigma-Aldrich)-based staining method is reasonably accurate as previously described, and in the majority of our experiments we tried to keep the band intensity within the linear range estimated in the previous study by adjusting the range of reaction time points (23).

In the assay to characterize the conversion of P2 to the 3-mer product (P3), ATP was supplied as the only NTP substrate and a higher P2 final concentration (95 μM) was used to achieve multiple turnovers within an applicable reaction duration. In a typical P2-to-P3 conversion assay, 50, 150, 300, 500, 1000 and 2000 μM ATP concentrations were tested. For quantitative analyses, to minimize the calculation error derived from gel-to-gel intensity variations and estimate the relative reaction rate of WT and its variant, we used a fixed amount (15 μl at 2 μM) of a chemically synthesized 8-mer (P8) RNA as a quantitation standard (STD) on both sides of each gel to correlate band intensities. The standardized P3 intensities were then used to estimate individual reaction rate through linear regression, and the calculated reaction rates under different ATP concentrations were fitted to the Michaelis-Menten equation to estimate the catalytic rate constant k_{cat} and the Michaelis constant $K_{M,ATP}$.

RESULTS

Crystal structure of the CSFV NS5B N-91 contains a relatively complete PE

Beyond the RdRP catalytic core, the about 710-residue pestivirus NS5B contains a 90-residue N-terminal domain (NTD) and a 24-residue C-terminal membrane anchoring helix (31,32). Previously reported pestivirus NS5B structures include RdRP-only structures of BVDV and NTD-containing structures of CSFV, but these structures only have a portion of the PE C-terminal tail resolved (17,18,33). With an aim to reveal a more complete picture of pestivirus NS5B PE, we constructed N-terminal and C-terminal truncated forms of CSFV NS5B and attempted crystallization. Among them, the N-91 construct with the NTD removed from the WT backbone (Shimen strain) was crystallized and yielded a 3.1-Å resolution structure (Table 1 and Figure 1B). The N-91 structure contains one NS5B molecule in the crystallographic asymmetric unit, and is largely consistent with the RdRP core in the NTD-containing CSFV NS5B WT structure (PDB entry: 5YF5) (18), with a root-mean-square deviation (RMSD) value of 0.9 Å (N-91 as the reference, 96% residue coverage). In the N-91 structure, 40 out of the 604 residues are unresolved (unresolved residue range: 91–92, 105–107, 119–133, 272–277, 392–394, 533–537 and 689–694).

In previously reported pestivirus NS5B structures, PE C-terminal tail residues 665–672 (PDB entry: 2CJQ)/665–674 (PDB entry: 1S4F), 665–670 (PDB entries 5YF5 and 5YF6), 665–678 (PDB entry: 5Y6R) of the BVDV, CSFV Shimen strain, CSFV Eystrup strain were resolved, respectively (17,18,33) (Figure 1C). Residues 665–670 formed a β-strand in these structures, and run antiparallel to residues 580–586 of the PE loop. In the latter CSFV structure, residues 673–678 folded back toward the upstream direction (according to polymerase synthesis), interacted with the palm, and only loosely associated with the rest of the thumb (33) (Figure 1C). By contrast, the N-91 structure showed a relatively complete picture of PE with residues 665–688 of the C-terminal tail resolved (Figure 1C and D). Residues 673–683 in this structure form antiparallel β-type substructures and interact with the rest of the thumb, making the PE an integrated structural element (Figure 1D and E).

Structural dynamics of the C-terminal tail may be critical for CSFV RdRP *de novo* initiation

The structural feature of PE observed in the N-91 construct evoked us to assess the contribution of structural dynamics of C-terminal tail to *de novo* initiation and to find out the regions required for this critical activity. We therefore made a set of point mutations at a conserved glycine residue (G671) critical for maintaining the first β-turn and presumably necessary for function-related conformational changes of the C-terminal tail (Figure 1E and Table 2). Previously established dinucleotide (P2)-driven RdRP assays were carried out to assess the effect on *de novo* initiation brought by these mutations (18,23,34), while the NTP-driven reactions were not chosen due to lower activity and product heterogeneity (18). In the presence of only ATP, WT NS5B was able to incorporate one AMP to form a 3-mer product (P3). This P3-containing complex is relatively unstable and the complex therefore can undergo multiple turnovers and continuously carry out the P2-to-P3 conversion if P2 and ATP are sufficient. Hence, this assay can be used to directly evaluate initiation activities (23). At 95 μM P2 and 300 μM ATP concentrations and 30°C, P3 production level was reduced for all mutants at the 45-min time point to 5–81% of the WT level (Figure 2B, compare lane 2 with lanes 3–8). In the presence of ATP and UTP, WT NS5B was able to initiate the synthesis, make the transition to elongation, and form a 9-mer product (P9)-containing elongation complex (EC9) with a half-life about one week (18). Therefore, the EC9 formation following a single-turnover mode with its amount saturated at a 1:1 molar ratio of P9:T30 ideally. At the 45-min reaction time point and under a relatively saturating NTP concentration (300 μM) and 30°C, all mutants were able to synthesize the P9 product, with the P9 amount being 18–90% of the WT level (Figure 2C, compare lane 12 with lanes 13–18). The smaller P9 amount difference between

Table 2. A list of CSFV NS5B constructs and initiation kinetic parameters for representative constructs.

Construct	Description	Rel. k_{cat} (min^{-1})	$K_{M,ATP}$ (μM)	Rel. $k_{cat}/K_{M,ATP}$ ($\mu M^{-1} \cdot min^{-1}$)
WT	1–694	12.4 ± 0.6[a]	426 ± 44[a]	0.029 ± 0.003[b]
G671P	1–694 w/ G671P	1.8 ± 0.1	469 ± 51	0.004 ± 0.001[c]
G671A	1–694 w/ G671A	6.0 ± 0.1	171 ± 13	0.035 ± 0.003
G671V	1–694 w/ G671V	4.5 ± 0.3	264 ± 49	0.017 ± 0.003
G671L	1–694 w/ G671L	5.5 ± 0.7	703 ± 158	0.008 ± 0.002
G671F	1–694 w/ G671F	5.3 ± 0.5	320 ± 73	0.017 ± 0.004
G671W	1–694 w/ G671W	4.8 ± 0.5	264 ± 70	0.018 ± 0.005
C-689	1–689	8.0 ± 0.7	290 ± 68	0.028 ± 0.007
C-682	1–682	9.1 ± 1.6	418 ± 167	0.022 ± 0.010
C-680	1–680	9.2 ± 1.3	591 ± 169	0.016 ± 0.005
C-678	1–678	1.7 ± 0.1	262 ± 55	0.007 ± 0.002
C-676	1–676	N/D[d]	N/D	N/D
C-674	1–674	N/D	N/D	N/D
C-672	1–672	N/D	N/D	N/D
N-91	91–694	N/D	N/D	N/D

[a]Fitting errors from the Michaelis-Menten curve fitting were provided.
[b]Errors of relative catalytic efficiency were propagated from the fitting errors of relative k_{cat} and $K_{M,ATP}$.
[c]0.001 was used for the propagated error that is lower than 0.001.
[d]Not determined.

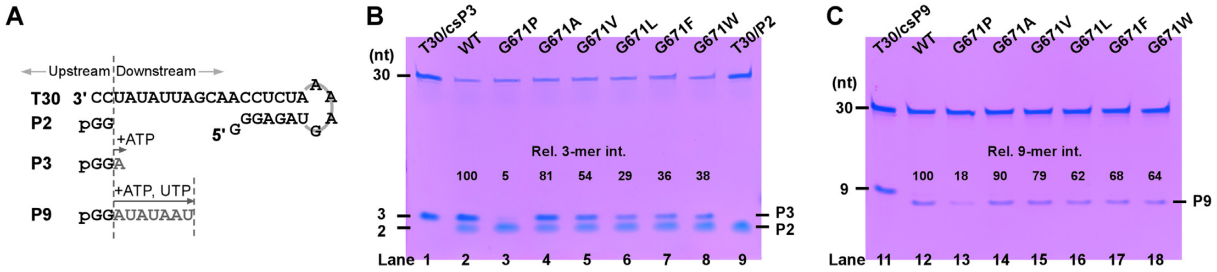

Figure 2. Mutations at residue G671 in the C-terminal tail impaired CSFV NS5B initiation activity. (**A**) A schematic diagram of RNA construct T30/P2 used in the RdRP assays and the reaction flow chart of the P2-to-P3 conversion and EC9 formation. When ATP or ATP/UTP were supplied as the only NTP substrate(s), the T30 template directed 1- or 7-nucleotide extension (gray) of the P2 (black) to produce 3-mer (P3) or 9-mer (P9) products. (**B**, **C**) Comparison of the WT CSFV NS5B and its G671 mutants in the P2-to-P3 conversion (B) and EC9 formation (C). The relative intensity of P3 or P9 was used to estimate polymerase activities (the values for WT were set to 100). A chemically synthesized 5′-phosphorylated trinucleotide GGA (csP3, identical to P3), P2, and a chemically synthesized 9-mer (csP9, 5′-hydroxyl, sequence identical to P9) were mixed with T30 at a molar ratio of 5:1, 23.75:1 and 1.25:1, respectively, to obtain T30/csP3, T30/P2, T30/csP9 mixtures as migration markers (lanes 1, 9 and 11). Note that csP9 bearing a hydroxyl group at the 5′-end migrated slower than P9 bearing a 5′-phosphate.

the WT and mutants suggests that all T30 templates had formed EC9 with the WT enzyme at the tested time point. Among these mutations, G671P had the greatest effect, consistent with the least backbone flexibility of the proline. The impairment of initiation brought by mutation at G671 suggests that either the G671-containing β-turn observed in the N-91 structure or a conformational change mediated by this glycine residue is essential for pestivirus RdRP *de novo* initiation.

Mutations at CSFV NS5B G671 resulted in up to 7-fold reduction in initiation efficiency primarily by affecting k_{cat}

To dissect the specific effect on enzymatic properties brought by mutation at residue G671, we first chose WT NS5B and the mutant G671P with the least backbone flexibility and compared their behaviors in the P2-to-P3 conversion assay. Catalytic rates under a series of ATP concentrations for each construct were estimated following an experimental setting established in a DENV study also characterizing dinucleotide-driven initiation (23) (Supplementary Figure S1). These initiation rates were then used to determine the catalytic rate constant k_{cat} and Michaelis constant $K_{M,ATP}$ of both constructs (Figure 3A and B, also see Materials and Methods). By optimizing the reaction time points selection for each NTP concentration and each construct, the 3-mer band intensities were controlled to be within the linear range of the Stains-All-based staining method to facilitate quantitation accuracy. For both constructs, we observed a substrate inhibition effect at 2 mM ATP concentration, and the reaction rates under this concentration were not included in the fitting routines. Strikingly, the initiation k_{cat} of the G671P mutant (1.8 ± 0.1 min^{-1}) is only about one-seventh of the WT value (12.4 ± 0.6 min^{-1}), while the Michaelis constant for the initiating NTP ($K_{M,ATP}$) were not much affected (469 ± 51 μM versus 426 ± 44 μM). In a *Picornaviridae* coxsackievirus B3 (CV B3) study, ATP but not other NTPs was found to bind at an allosteric site and act as non-competitive inhibitors of RdRP (35). When noncognate CTP or 2′-deoxy-CTP (2dCTP) were provided at 1 mM concentration in the P2-to-P3 conversion assay, the ATP self-inhibitory effect was not reduced, while the reduced levels of P3 indicates competitive inhibition (Figure 3C and D and Supplementary Figure S2). These observations suggest

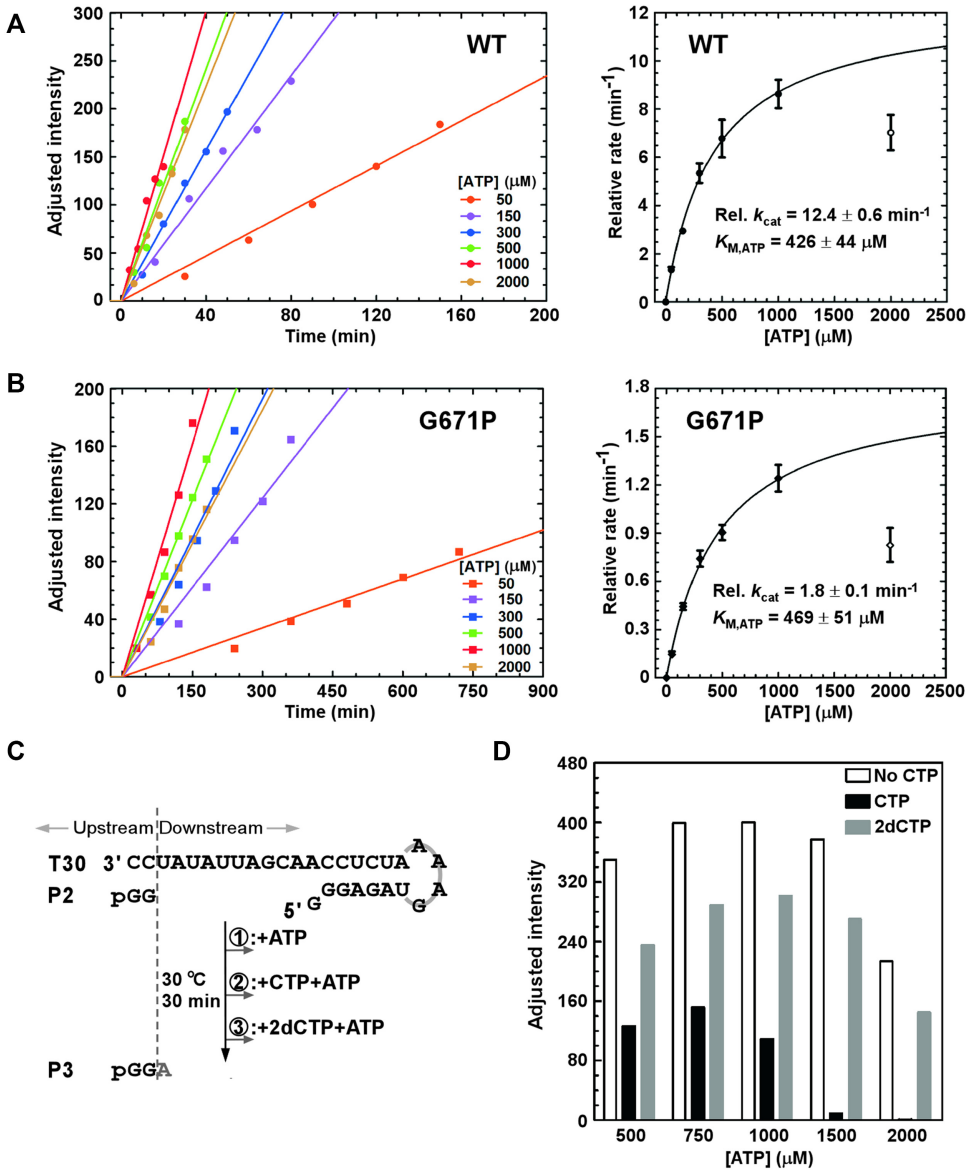

Figure 3. A comparison of initiation kinetics of the WT CSFV NS5B and the G671P mutant. (A, B) The initiation kinetics analyses for the WT (**A**) and G671P (**B**) construct. Left: linear regression of P3 relative intensities at six ATP concentrations. Right: Michaelis–Menten curve fitting of the relative reaction rate as a function of ATP concentration for WT and G671P. The data points indicated by empty symbols were not included in the fitting due to the inhibitory effect observed under 2 mM ATP concentration. The value of relative rate constants (Rel. k_{cat}) and Michaelis constants ($K_{M,ATP}$) with fitting errors were indicated. Each data series of the Michaelis–Menten fitting was taken from three individual experimental sets. Average number, standard deviation (SD) are shown, and gels from one set are shown in Supplementary Figure S1. (**C**) The reaction flow chart of the assay verifying the ATP inhibitory effect. The ATP-driven P2-to-P3 conversion was monitored with noncognate CTP or 2′-deoxy-CTP (2dCTP) supplied in comparison with the ATP only reaction. (**D**) A bar chart showing the ATP inhibitory effect both in the absence and presence of noncognate CTP/2dCTP. The relative intensity of P3 was used for quantitation with the average intensity value of the STD bands set to 100, while the gel image is shown in Supplementary Figure S2.

that the allosteric ATP binding site identified in the CV B3 study may also present in CSFV RdRP.

We next determined k_{cat} and $K_{M,ATP}$ values for other G671 mutants. It turned out that all these mutants exhibited an apparent decrease (about 2–3-fold) in k_{cat} if compared with the WT value, while the $K_{M,ATP}$ values were only moderately affected (40–165% of the WT-level, Figure 4A, Table 2). While the proline mutation appeared most influential due to the unique property of proline in backbone geometry, the effect on k_{cat} by the non-proline mutations are not much affected by the size of the side chain mutated. For example, the initiation k_{cat} values were 6.0 ± 0.1 min^{-1}, 5.5 ± 0.7 min^{-1} and 4.8 ± 0.5 min^{-1} for the G671A (small size), G671L (medium size) and G671W (large size) mutants, respectively. If using $k_{cat}/K_{M,ATP}$ value to assess catalytic efficiency, all G671 mutants, except for G671A, had values lower than the WT with the lowest being G671L (Table 2). These data are largely consistent with the fact that proline and glycine being the residues with the least and most backbone flexibility, indicating that the backbone

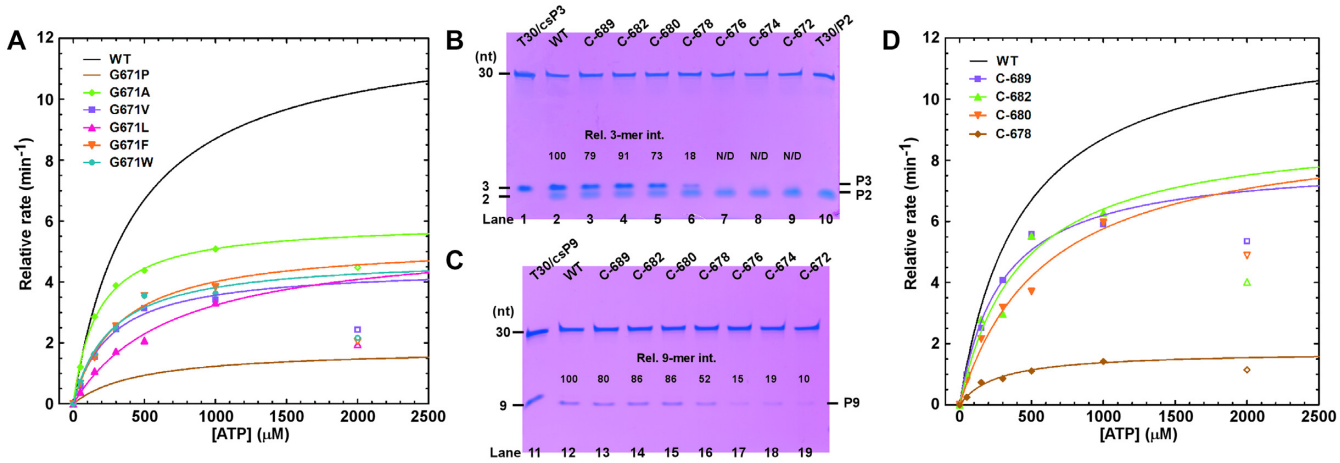

Figure 4. Characterization of the initiation kinetics of additional G671 mutants and C-terminal truncated constructs of CSFV NS5B. (**A**) Michaelis–Menten curve fitting of the relative reaction rate as a function of ATP concentration for additional G671 mutants. The fitted curves of WT (black) and G671 (olive) data taken from Figure 3 are shown for comparison. (**B**) Comparison of the WT CSFV NS5B and its C-terminal truncated mutants in the P2-to-P3 conversion (B) and EC9 formation (**C**). The relative intensity of P3 or P9 was used to estimate polymerase activities (the values for WT were set to 100). T30/csP3 (5′-phosphate), T30/P2, T30/csP9 (5′-hydroxyl) markers were provided as illustrated in Figure 2B and C. N/D: not determined. (**D**) Michaelis–Menten curve fitting of the relative reaction rate as a function of ATP concentration for C-terminal truncated mutants. The fitted curve of WT (black) data taken from Figure 3 are shown for comparison. The data points in panels A and C indicated by empty symbols were not included in the fitting.

flexibility at residue G671 and related local conformational changes is critical for pestivirus NS5B initiation.

Residues 681–694 of the C-terminal tail are not critical for CSFV RdRP *de novo* initiation

The importance of residue G671 in CSFV RdRP initiation strongly suggests that residues in the C-terminal part of the PE C-terminal tail also contribute to RdRP initiation. In the N-91 structure, the observed conformation of PE C-terminal tail is stabilized by interactions from a neighboring NS5B molecule in the crystal lattice. The primary solution conformation of the C-terminal tail, or its initiation-competent conformation as discussed below, are still unclear. In order to determine the specific region within the C-terminal tail required for initiation, a set of six C-terminal truncated CSFV NS5B mutants were compared with the WT enzyme in both the P2-to-P3 conversion assay and the EC9 formation assay (Figure 4 and Table 2). Consistent with our previous study (18), constructs C-689, C-682 and C-680 produced comparable amount of P3 product as the WT at the 45-min time point (Figure 4B, compare lanes 3–5 with lane 2). By contrast, construct C-678 clearly yielded lower-than-WT amount of P3, while P3 production by constructs C-676, C-674 and C-672 was hardly detected (Figure 4B, compare lanes 6–9 with lane 2). The results of the EC9 formation assay were similar to those of the P2-to-P3 conversion assay, with only C-678, C-676, C-674 and C-672 showing notable impact on P9 production (Figure 4C, compare lanes 16–19 with lanes 12).

Likewise, we next determined the k_{cat} and $K_{M,ATP}$ for four representative C-terminal truncated constructs using the P2-to-P3 conversion assay (Figure 4D, Table 2). Constructs C-689, C-682 and C-680 that behaved similarly to WT in single-time-point tests had k_{cat} values close to the WT value (65–74%). By contrast, the k_{cat} value of the C-678 construct was much lower than that of the WT (1.7 ± 0.1 min^{-1}, 14%), and is comparable to that of G671P. Consistent with the G671 point mutations, the $K_{M,ATP}$ values were comparable to that of the WT (62–139% of the WT-level). The $k_{cat}/K_{M,ATP}$ values of these truncation decrease from 97% (C-689), to 55% (C-680), and further to 24% (C-678) of the WT-level with a correlation with the truncation length. Taken together, these data indicate that residues 665–680, corresponding to the N-terminal β-hairpin of the C-terminal tail observed in the N-91 structure, are critical for CSFV RdRP initiation.

CSFV NS5B exhibits terminal initiation preference as other *Flaviviridae* RdRPs

RdRP initiation from the 3′-terminus of the template ensures faithful passage of RNA length during viral genome replication. It is therefore conceivable that PEs may have been evolved to prefer terminal initiation over internal initiation as demonstrated in HCV NS5B (36). Structurally, terminal initiation likely requires PE to reach the –1 site (or to occupy the –2 site) to restrict the placement of the 3′-end of the template RNA as observed in bacteriophage ϕ6 RdRP IC (7). However, for all pestivirus NS5B structures solved to date, the ordered part of PE appears not long enough to reach the –1 site. By contrast, the flavivirus NS5 PE has a length similar to the ϕ6 RdRP PE (20,37). This raises the question whether the pestivirus NS5B prefers terminal initiation as its PE may indeed not be able to reach the –1 site. We therefore carried out a comparative study using three representative *Flaviviridae* RdRPs, CSFV NS5B, HCV NS5B, and DENV2 NS5 to qualitatively assess their terminal initiation preference (Figure 5). Three additional template RNAs, all directing internal initiation if annealed with P2, were used in the P2-to-P3 conversion assays in comparison with the terminal initiating T30 (Figure 5A). Very interestingly, the results clearly indicated a terminal initiation preference of CSFV NS5B. Specifically, internal

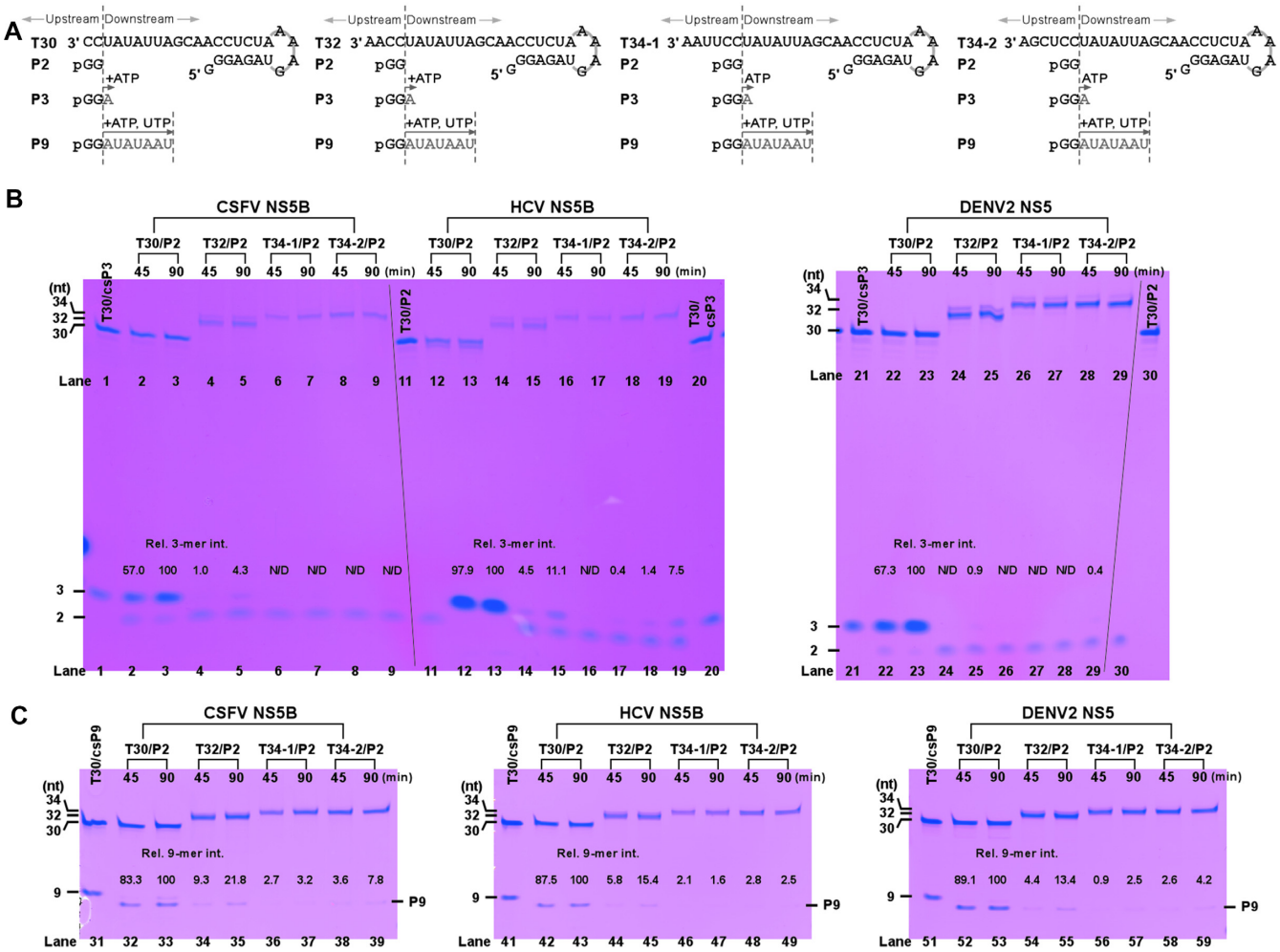

Figure 5. Terminal initiation preference assessment of three representative *Flaviviridae* RdRPs. (**A**) A diagram of the terminal and internal initiation RdRP assays. Construct T30/P2 was used for terminal initiation, while T32/P2, T34-1/P2 and T34-2/P2 were used for the internal initiation. When ATP or ATP/UTP were supplied as the only NTP substrate(s), every template strand directed 1- or 7-nucleotide extension (gray) of the P2 (black) to produce 3-mer (P3) or 9-mer (P9) products. (B, C) Comparison of terminal initiation and internal initiation in representative *Flaviviridae* RdRPs in the multiple-turnover P2-to-P3 conversion (**B**) and the single-turnover EC9 formation (**C**) assays. T30/csP3 (5′-phosphate), T30/P2, T30/csP9 (5′-hydroxyl) markers were provided as illustrated in Figures 2B, C and 4B, C. The 90-min band intensity of P3 or P9 derived from the T30/P2 construct was set to 100 to aid the assessment of terminal preference for each enzyme.

initiation level on T32 was much lower than that of terminal initiation on T30, while initiation from the T34-1 or T34-2 was nearly non-detectable (Figure 5B, compare lanes 4–9 with lanes 2–3). These results are largely consistent with those obtained using HCV NS5B and DENV2 NS5, in spite of variation in both terminal and internal initiation levels across different RdRPs (Figure 5B, compare lanes 2–9 with lanes 12–19 and 22–29). These data strongly suggest that the terminal initiation preference is probably conserved in *Flaviviridae* RdRPs, even though the observed PE substructure architectures clearly differ. Moreover, initiation from the sixth/seventh positions from the 3′-end of the template appeared even more difficult than that from the fourth/fifth positions for all three RdRPs (Figure 5B, compare lanes of T34-1/T34-2 with lanes of T32), further supporting the terminal initiation preference for these enzymes. We also tested EC9 formation on these RNA constructs with all three RdRPs, the results were consistent with those of the P2-to-P3 conversion with clearly much higher P9 production from the T30 than that from other templates (Figure 5C).

DISCUSSION

The preference of terminal initiation of CSFV NS5B and the about 9-Å spatial separation of the pestivirus RdRP PE substructure and the initiation site together strongly suggest that a conformational change of PE is required to fulfill efficient terminal initiation. Among representative PE containing viral RdRPs, those of bacteriophage ϕ6, influenza viruses, JEV/DENV can reach the initiation site by comparing the ϕ6 RdRP IC and corresponding apo RdRP structures (9,19,20) (Figure 6A–C). The PE of HCV RdRP protrudes into the initiation site and sterically incompatible to the RNA template and initiating NTPs in the apo RdRP structure (11), while the PE C-terminal tail folds back to-

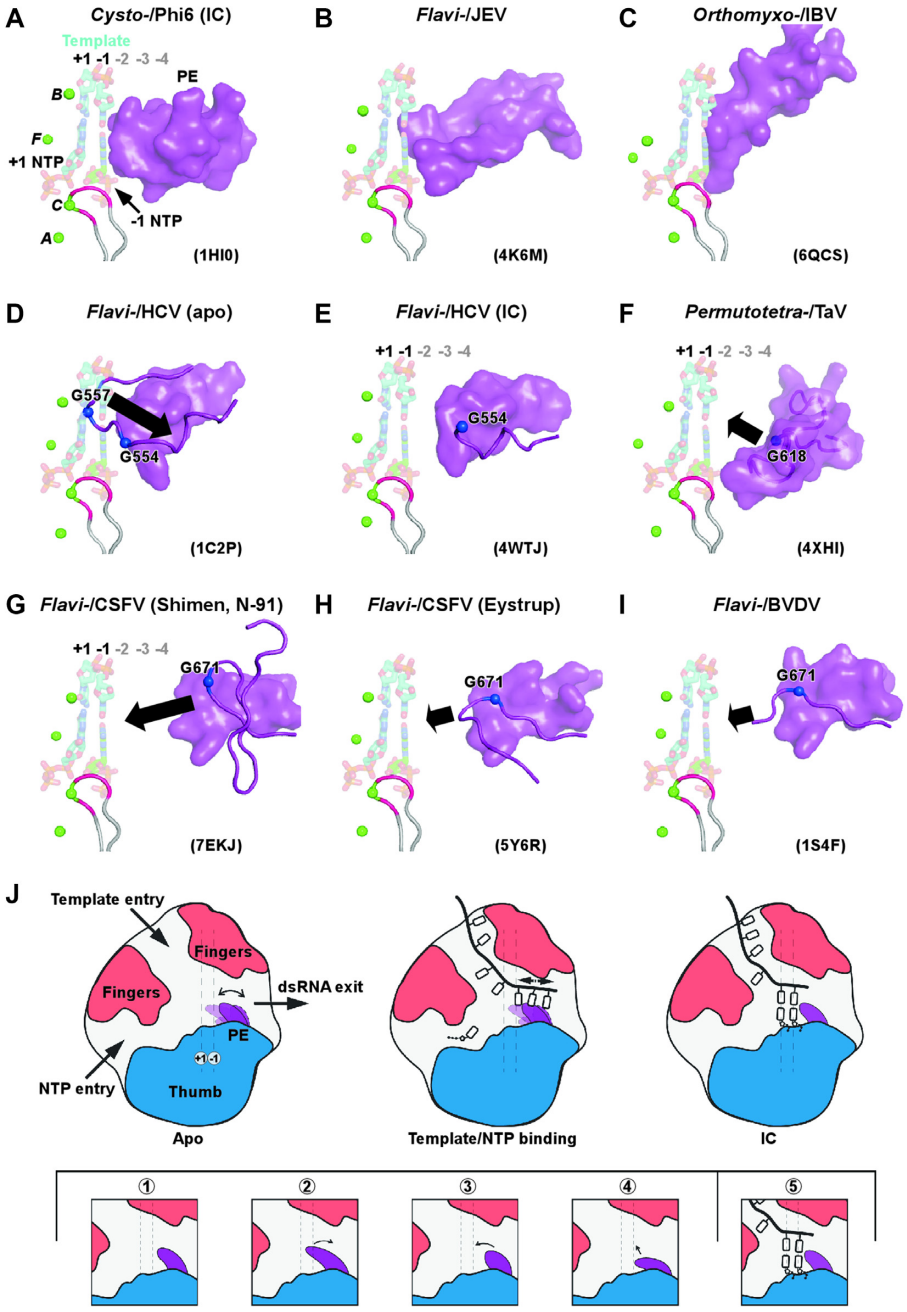

Figure 6. A structural comparison of RdRP PE suggests an induced-fit mechanism for *de novo* initiation. (**A**–**I**) A comparison of PEs in representative viral RdRPs. All structures are superimposed by the least-square method using their motif C residues and are presented individually. Motif C (cartoon representation) and the α-carbon of the four invariant RdRP residues (green spheres, a motif A aspartate, a motif B glycine, a motif C aspartate, and a motif F arginine) from each structure and the RNA template and initiating NTPs from the bacteriophage ϕ6 IC structure are used as references. One-segment PEs are shown in surface representation except that TaV RdRP PE is shown as a combination of semi-transparent surface and cartoon representations. For two-segment PEs, the thumb insertion and the C-terminal tail are shown in surface and cartoon representations, respectively. The α-carbon atoms of PE glycine residues that may play critical roles in the proposed induced-fit conformational changes are shown as blue spheres. The estimated upstream nucleotide positions are shown in gray. Block arrows indicate probable conformational changes to achieve *de novo* initiation. Note that the HCV IC is a dinucleotide-derived structure with PE reaching the –2 position as shown in Figure 1A. Under NTP-driven initiation situation, its PE is expected to further reach the –1 position. (**J**) A working model of the induced-fit mechanism of *de novo* RdRP PE at initiation. The apo RdRP can have versatile PE conformations (Top left image and bottom images 1–4). Upon template RNA and NTP binding, an induced-fit process allows precise placement of the template terminus, while stabilizing the initiating NTPs (Top middle image of the top row), resulting in efficient and precise initiation in an IC (top right image and bottom image 5). The arrows in the bottom row indicate required conformational changes of PE to reach its initiation-competent state.

ward the upstream in the dinucleotide-derived HCV RdRP IC structure (8) (Figure 6D and E). The PE of the *Permutotetraviridae* Thosea asigna virus (TaV) only reaches the product side of the initiation site but not the template side in the corresponding apo RdRP structure (38), and a conformational change to bring the PE toward the template side is likely needed for initiation (Figure 6F). The pestivirus RdRP PE, including that observed in the N-91 structure, exhibits conformational dynamics for residues beyond the G671 in PE C-terminal tail (Figure 6G–I). However, none of the observed PE conformations having the PE reach the initiation site. The functional importance of G671 and residues 665–680 in CSFV initiation evokes us to propose that a conformational change around residue G671 may bring critical residues within the 672–680 region toward the initiation site to achieve a similar architecture observed in ϕ6 and HCV RdRP IC structures. Very interestingly, glycine residues also exist in HCV and TaV RdRP PEs, presumably to facilitate aforementioned local conformational changes (Figure 6D–F). Note that *Flaviviridae* RdRPs typically exhibit low solubility under low ionic strength required for efficient initiation in *in vitro* assays (18,23,30,34), thus making it impractical to use optics-derived approaches to detect the conformational changes upon the proposed induced-fit process. Nevertheless, future efforts in solving corresponding RdRP IC structures are likely required to reveal precise structural rearrangements proposed here for CSFV and TaV.

By solving a pestivirus RdRP structure with a relatively intact PE and by functionally identifying critical residue/region for PE structural dynamics and *de novo* initiation, our work helps reconcile the substructure diversity of viral RdRP PEs and their functional conservation of terminal *de novo* initiation by pointing out that PE can fulfill *de novo* initiation in an induced-fit manner (Figure 6J). The structural dynamics of PE is also compatible with the consensus view that PE needs to withdraw from the initiation site upon the transition to elongation that is still awaiting critical structural evidence.

DATA AVAILABILITY

Atomic coordinates and structure factors for the reported crystal structure have been deposited with the Protein Data Bank under accession code 7EKJ.

SUPPLEMENTARY DATA

Supplementary Data are available at NAR Online.

ACKNOWLEDGEMENTS

We thank Dr Zishu Pan for providing cloning materials for the CSFV polymerase gene (Shimen strain), Dr Meihua Wang for preparing the HCV NS5B, Dr Jiqin Wu and Xinyu Wang for preparing the DENV NS5, Dr Peng Bi, Liu Deng and Qiaojie Liu for laboratory assistance, and the Core Facility and Technical Support, Wuhan Institute of Virology for access to instruments.

Author contributions: P.G., conceived the research; W.L. performed the crystallographic experiments; B.-Y.Z. and W.L. performed the biochemical experiments; H.J. prepared the RNA templates for testing internal initiation; W.L., G.L. and P.G. analyzed the structural data; B.-Y.Z., W.L. and P.G. analyzed the biochemical data. B.Y.Z., W.L., G.L. and P.G. wrote the manuscript, and all authors approved the manuscript content.

FUNDING

National Key Research and Development Program of China [2018YFD0500100 to P.G.]; National Natural Science Foundation of China [32070185, 31670154 to P.G., 31802147 to G.L.]; Chinese Academy of Sciences Funds: Special Research Assistant Program [2021000042 to W.L.]; Advanced Customer Cultivation Project of Wuhan National Biosafety Laboratory [2018ACCP-MS06, 2021ACCP-MS10 to P.G.]. Funding for open access charge: National Key Research and Development Program of China [2018YFD0500100]; National Natural Science Foundation of China [32070185, 31802147].

Conflict of interest statement. None declared.

REFERENCES

1. Gralla,J.D., Carpousis,A.J. and Stefano,J.E. (1980) Productive and abortive initiation of transcription in vitro at the lac UV5 promoter. *Biochemistry*, **19**, 5864–5869.
2. Martin,C.T., Muller,D.K. and Coleman,J.E. (1988) Processivity in early stages of transcription by T7 RNA polymerase. *Biochemistry*, **27**, 3966–3974.
3. Arnold,J.J. and Cameron,C.E. (2000) Poliovirus RNA-dependent RNA polymerase (3D(pol)). Assembly of stable, elongation-competent complexes by using a symmetrical primer-template substrate (sym/sub). *J. Biol. Chem.*, **275**, 5329–5336.
4. Paul,A.V. and Wimmer,E. (2015) Initiation of protein-primed picornavirus RNA synthesis. *Virus Res.*, **206**, 12–26.
5. Imbert,I., Guillemot,J.C., Bourhis,J.M., Bussetta,C., Coutard,B., Egloff,M.P., Ferron,F., Gorbalenya,A.E. and Canard,B. (2006) A second, non-canonical RNA-dependent RNA polymerase in SARS coronavirus. *EMBO J.*, **25**, 4933–4942.
6. Reich,S., Guilligay,D., Pflug,A., Malet,H., Berger,I., Crepin,T., Hart,D., Lunardi,T., Nanao,M., Ruigrok,R.W. *et al.* (2014) Structural insight into cap-snatching and RNA synthesis by influenza polymerase. *Nature*, **516**, 361–366.
7. Butcher,S.J., Grimes,J.M., Makeyev,E.V., Bamford,D.H. and Stuart,D.I. (2001) A mechanism for initiating RNA-dependent RNA polymerization. *Nature*, **410**, 235–240.
8. Appleby,T.C., Perry,J.K., Murakami,E., Barauskas,O., Feng,J., Cho,A., Fox,D. 3rd, Wetmore,D.R., McGrath,M.E., Ray,A.S. *et al.* (2015) Viral replication. Structural basis for RNA replication by the hepatitis C virus polymerase. *Science*, **347**, 771–775.
9. Kouba,T., Drncova,P. and Cusack,S. (2019) Structural snapshots of actively transcribing influenza polymerase. *Nat. Struct. Mol. Biol.*, **26**, 460–470.
10. Wu,J., Liu,W. and Gong,P. (2015) A structural overview of RNA-dependent RNA polymerases from the Flaviviridae family. *Int. J. Mol. Sci.*, **16**, 12943–12957.
11. Lesburg,C.A., Cable,M.B., Ferrari,E., Hong,Z., Mannarino,A.F. and Weber,P.C. (1999) Crystal structure of the RNA-dependent RNA polymerase from hepatitis C virus reveals a fully encircled active site. *Nat. Struct. Biol.*, **6**, 937–943.
12. Thompson,A.A. and Peersen,O.B. (2004) Structural basis for proteolysis-dependent activation of the poliovirus RNA-dependent RNA polymerase. *EMBO J.*, **23**, 3462–3471.
13. te Velthuis,A.J. (2014) Common and unique features of viral RNA-dependent polymerases. *Cell. Mol. Life Sci.*, **71**, 4403–4420.
14. Jia,H. and Gong,P. (2019) A structure-function diversity survey of the RNA-Dependent RNA polymerases from the positive-Strand RNA viruses. *Front. Microbiol.*, **10**, 1945.

15. Bruenn,J.A. (2003) A structural and primary sequence comparison of the viral RNA-dependent RNA polymerases. *Nucleic Acids Res.*, **31**, 1821–1829.
16. Gorbalenya,A.E., Pringle,F.M., Zeddam,J.L., Luke,B.T., Cameron,C.E., Kalmakoff,J., Hanzlik,T.N., Gordon,K.H. and Ward,V.K. (2002) The palm subdomain-based active site is internally permuted in viral RNA-dependent RNA polymerases of an ancient lineage. *J. Mol. Biol.*, **324**, 47–62.
17. Choi,K.H., Groarke,J.M., Young,D.C., Kuhn,R.J., Smith,J.L., Pevear,D.C. and Rossmann,M.G. (2004) The structure of the RNA-dependent RNA polymerase from bovine viral diarrhea virus establishes the role of GTP in de novo initiation. PNAS, **101**, 4425–4430.
18. Liu,W., Shi,X. and Gong,P. (2018) A unique intra-molecular fidelity-modulating mechanism identified in a viral RNA-dependent RNA polymerase. *Nucleic Acids Res.*, **46**, 10840–10854.
19. Yap,T.L., Xu,T., Chen,Y.L., Malet,H., Egloff,M.P., Canard,B., Vasudevan,S.G. and Lescar,J. (2007) Crystal structure of the dengue virus RNA-dependent RNA polymerase catalytic domain at 1.85-angstrom resolution. *J. Virol.*, **81**, 4753–4765.
20. Lu,G. and Gong,P. (2013) Crystal structure of the full-length japanese encephalitis virus NS5 reveals a conserved methyltransferase-Polymerase interface. *PLoS Pathog.*, **9**, e1003549.
21. Chiu,J., March,P.E., Lee,R. and Tillett,D. (2004) Site-directed, ligase-independent mutagenesis (SLIM): a single-tube methodology approaching 100% efficiency in 4 h. *Nucleic Acids Res.*, **32**, e174.
22. Papworth,C.B., Bauer,J.C., Braman,J. and Wright,D.A. (1996) Site-directed mutagenesis in one day with >80% efficiency. *Strategies*, **9**, 3–4.
23. Wu,J., Ye,H.Q., Zhang,Q.Y., Lu,G., Zhang,B. and Gong,P. (2020) A conformation-based intra-molecular initiation factor identified in the flavivirus RNA-dependent RNA polymerase. *PLoS Pathog.*, **16**, e1008484.
24. Otwinowski,Z. and Minor,W. (1997) In: *Processing of X-ray Diffraction Data Collected in Oscillation Mode*. Academic Press, NY.
25. McCoy,A.J., Grosse-Kunstleve,R.W., Adams,P.D., Winn,M.D., Storoni,L.C. and Read,R.J. (2007) Phaser crystallographic software. *J. Appl. Crystallogr.*, **40**, 658–674.
26. Adams,P.D., Afonine,P.V., Bunkoczi,G., Chen,V.B., Davis,I.W., Echols,N., Headd,J.J., Hung,L.W., Kapral,G.J., Grosse-Kunstleve,R.W. *et al.* (2010) PHENIX: a comprehensive Python-based system for macromolecular structure solution. *Acta Crystallogr. D, Biol. Crystallogr.*, **66**, 213–221.
27. Emsley,P., Lohkamp,B., Scott,W.G. and Cowtan,K. (2010) Features and development of Coot. *Acta Crystallogr. D, Biol. Crystallogr.*, **66**, 486–501.
28. Theobald,D.L. and Wuttke,D.S. (2006) THESEUS: maximum likelihood superpositioning and analysis of macromolecular structures. *Bioinformatics*, **22**, 2171–2172.
29. Batey,R.T. and Kieft,J.S. (2007) Improved native affinity purification of RNA. *RNA*, **13**, 1384–1389.
30. Wu,J., Lu,G., Zhang,B. and Gong,P. (2015) Perturbation in the conserved methyltransferase-polymerase interface of flavivirus NS5 differentially affects polymerase initiation and elongation. *J. Virol.*, **89**, 249–261.
31. Lai,V.C., Kao,C.C., Ferrari,E., Park,J., Uss,A.S., Wright-Minogue,J., Hong,Z. and Lau,J.Y. (1999) Mutational analysis of bovine viral diarrhea virus RNA-dependent RNA polymerase. *J. Virol.*, **73**, 10129–10136.
32. Ferrari,E., Wright-Minogue,J., Fang,J.W., Baroudy,B.M., Lau,J.Y. and Hong,Z. (1999) Characterization of soluble hepatitis C virus RNA-dependent RNA polymerase expressed in *Escherichia coli*. *J. Virol.*, **73**, 1649–1654.
33. Li,W., Wu,B., Soca,W.A. and An,L. (2018) Crystal structure of classical swine fever virus NS5B reveals a novel N-terminal domain. *J. Virol.*, **92**, e00324-18.
34. Jin,Z., Leveque,V., Ma,H., Johnson,K.A. and Klumpp,K. (2012) Assembly, purification, and pre-steady-state kinetic analysis of active RNA-dependent RNA polymerase elongation complex. *J. Biol. Chem.*, **287**, 10674–10683.
35. Karr,J.P. and Peersen,O.B. (2016) ATP is an allosteric inhibitor of coxsackievirus B3 polymerase. *Biochemistry*, **55**, 3995–4002.
36. Hong,Z., Cameron,C.E., Walker,M.P., Castro,C., Yao,N., Lau,J.Y. and Zhong,W. (2001) A novel mechanism to ensure terminal initiation by hepatitis C virus NS5B polymerase. *Virology*, **285**, 6–11.
37. Lu,G. and Gong,P. (2017) A structural view of the RNA-dependent RNA polymerases from the Flavivirus genus. *Virus Res.*, **234**, 34–43.
38. Ferrero,D.S., Buxaderas,M., Rodriguez,J.F. and Verdaguer,N. (2015) The structure of the RNA-Dependent RNA polymerase of a permutotetravirus suggests a link between primer-dependent and primer-independent polymerases. *PLoS Pathog.*, **11**, e1005265.